

RESEARCH ARTICLE

Reverse-Current Induced Cascade Degradation in Ni–Ru Electrodes: Tracing the Path from Noble Metal Loss to Substrate Corrosion

Xukang Wang | Chenchen Feng | Lingao Deng | Chao Liu | Feifei Li | Luyu Yang | Zijian Gao | Tong Sun | Jiangong Zhu | Zhen Geng | Cunman Zhang | Liming Jin 

School of Automotive Studies and Clean Energy Automotive Engineering Center, Tongji University, Shanghai, China

Correspondence: Liming Jin (limingjin@tongji.edu.cn)

Received: 30 October 2025 | **Revised:** 26 November 2025 | **Accepted:** 27 November 2025

Keywords: accelerated stress test | alkaline water electrolysis | galvanic corrosion | multi-stage degradation | renewable energy | reverse current

Abstract

Long-term durability of Ni-based electrodes under renewable energy (RE) driven dynamic operation, remains a critical bottleneck in advancing the alkaline water electrolysis (AWE). Among various durability-related failure behaviors, degradation induced by reverse current (RC) has been largely overlooked, despite its growing relevance under fluctuating RE. Herein, we systematically elucidate a multistage degradation pathway of Ni–Ru electrodes (NR) under an accelerated stress test (AST). By combining full-process electrochemical monitoring with morphological and compositional analysis the pathway is summarized as follow: (i) the dense Ru layer is initially oxidized into rough and defective surface with high surface area, under the Ostwald ripening effect; (ii) promoted by the gradual formation of the Ni–Ru co-exposure to the electrolyte, the Ni substrate is subsequently galvanic corroded accompanied by partial Ru redeposition; (iii) through prolonged operation, both Ni and Ru are extensively oxidized and precipitated, eventually resulting in complete Ru depletion and structural collapse of Ni substrate. Based on this mechanistic understanding, we further investigate the effect of RC amplitude on degradation kinetics. Reducing the RC amplitude fraction from 20% to 0%, the initial Ru oxidation is effectively suppressed and following failure is thereby mitigated, with decreasing the degradation rate from 4.756 to 0.257 mV h⁻¹. These findings provide with fundamental insight into dynamic degradation evolution and offer practical mechanism for RC-tolerant electrode design.

1 | Introduction

With the rapid increase of social demand for green hydrogen production, alkaline water electrolysis (AWE) powered by renewable energy (RE) is gaining great attention as a scalable and cost-effective route. Promising implementation of RE-AWE is directly associated with the efficiency and stability of electrolysis,

which could be promoted by the core component electrode with enhanced catalytic activity and durability [1–10]. In particular, Ni-X electrode (X: Ru, Fe, Co et al.) has attracted great attention due to the high catalytic activity benefited from the intermetallic synergistic effect [11, 12], yet suffers from insufficient durability caused by severe degradation under dynamic operation powered by RE. In this regard, ascertaining the inducing

Abbreviations: AST, accelerated stress test; AWE, alkaline water electrolysis; BoT, begin of test; CV, cyclic voltammograms; EoT, end of test; EIS, electrochemical resistance spectroscopy; ECSA, electrochemical active area; EDS, Energy Dispersive X-ray Spectroscopy; ICP-MS, Inductively Coupled Plasma Optical Emission Spectrometry/Mass Spectrometry; LSV, linear sweep voltammetry; Ni, nickel; NR, Ni–Ru electrode; RE, renewable energy; RC, reverse current; Ru, ruthenium; RHE, reference hydrogen electrode; SHE, standard hydrogen electrode; SEM, scanning electron microscope; TEM, transmission electron microscope; XPS, X-ray photoelectron spectroscopy.

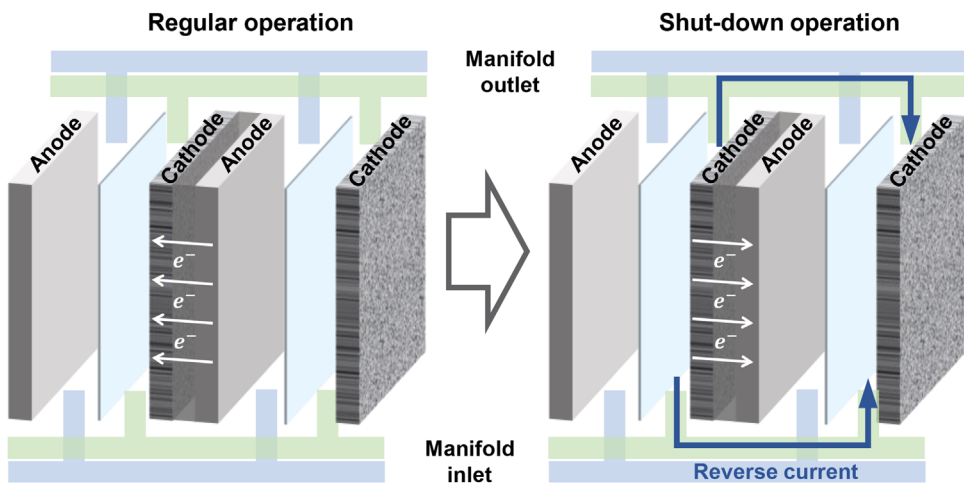


FIGURE 1 | Schematic description of RC formation after the rapid shut-down operation.

stresses from RE power and corresponding degradation-inducing mechanisms is extremely crucial. Reverse current (RC), resulting from the reverse self-discharge after the rapid shut down triggered, was reported to induce the degradation of electrode through converting the redox condition as shown in Figure 1 [13–28]. Furthermore, for the rapid shut-down operations are frequently triggered by the intermittent and fluctuating input, the RC-induced degradation is even accelerated in the long-term operation powered by RE. However, due to the restriction to constant condition in the previous studies, the RC-induced degradation is grossly neglected. Consequently, fundamental understanding of RC-induced degradation is critically required.

Kim et al. [29], and Holmin et al. [15], have simulated the RC-induced degradation of Ni-based cathode by directly applying the potential (1.6 V vs RHE for 30 min) and current density (640 mA cm^{-2} for 6 h) for oxygen evolution reaction (OER). Similar conclusions were acquired that the irreversible electrochemical oxidation was responsible for the RC-induced degradation. It is worth noting that with the oxidation proceeds, component of electrode and electrolyte changes as well, which indicates the existence of complicated degradation evolution during long-term operation. Yet the long-term RC-induced degradation have not been investigated in depth due to the excessive time required by the durability test and the enclosed property of the traditional “begin-end” test [30–34]. More importantly, the above-mentioned simulating RC durations are significantly higher than 1 min, which overlooked the high-frequency alternating property of practical RC operation. Because the durations of RC are influenced by multiple factors in the AWE system, up to date rare efforts have been done with applying practical RC profile to the degradation study. As a result, a more realistic durability study is urgently required to reveal the long-term RC-induced degradation behavior.

Herein, a “RC-like” accelerated stressed test (AST) protocol was employed to examine the RC-induced degradation of Ni-Ru electrodes (NR) in comparison to constant potential test (CP). The simulation approach was practical in that it utilized the repetitive alternation of regular condition and RC condition instead of directly maintaining the reversal condition. The AST profile demonstrates a high resolution of 1 s and the shortest

step duration among the available profiles, which enables us to maximize the long-term impact of RC during RE-AWE within a short test length. Additionally, a full-process monitoring method combining the electrochemical measurements with morphology and compositional characterizations was conducted to demonstrate the complete catalytic and structural degradation behavior. Results showed that NR after the AST exhibited a 214-mV overpotential increase at 400 mA cm^{-2} compared with that after CP, along with total Ru depletion and Ni substrate damaged. More in-depth, comprehensive analysis revealed that the degradation behavior of NR underwent a three-stage evolution. Initially, the dense Ru layer was oxidized and reformed into rough and defective surface under the Ostwald ripening effect. Subsequently, due to the surface defects, galvanic corrosion of Ni substrate was triggered by the Ni-Ru co-exposure to the electrolyte, accompanied with partial redeposition of Ru species. Eventually, through prolonged operation with the above electrochemical reactions, both Ni and Ru were extensively oxidized and precipitated, resulting in complete depletion of Ru and structural collapse of the Ni substrate. In addition, sensitivity of the degradation to the RC amplitude was investigated as well. Reducing the RC fraction from 20% to 0%, degradation rate was mitigated from 4.756 to 0.257 mV h^{-1} . Combined analysis manifested that the mitigation resulted from the suppress effect of lower RC to the initial Ru oxidation, which prevented the electrode from subsequent corrosion. These results provide with mechanistic reference for durable Ni-X electrode design to construct RE-AWE system. Ultimately, these lab-scale findings will promote industrial-scale electrolysis powered by renewable energies into reality.

2 | Results and Discussion

2.1 | Degradation Assessment

We applied an AST protocol with two-step square wave in a single cycle for totally 60 000 cycles, which simulated the alternation between regular operation (-1.3 V vs RHE for 2 s) and RC operation (0.5 V vs RHE for 1 s) as shown in Figure 2a,b. CP were applied as well for comparison to eliminate the influence of regular operation. NR were used as cathode and tested in

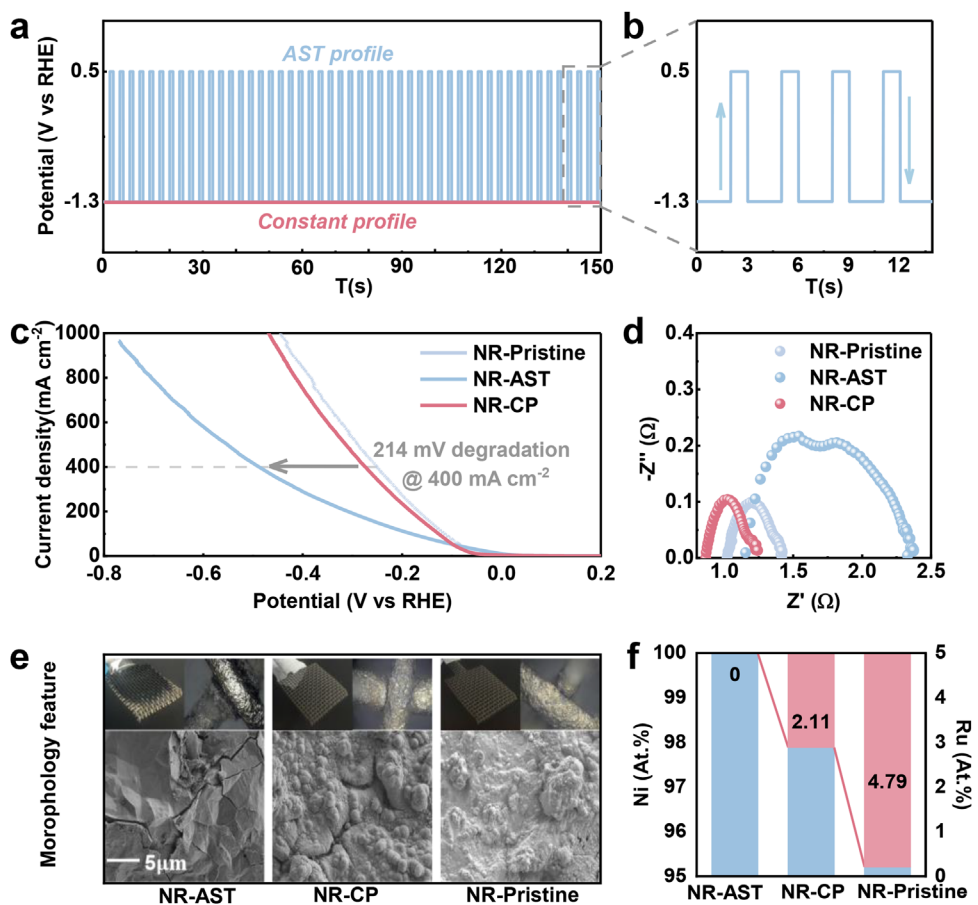


FIGURE 2 | Applied input profile and electrode degradation. (a,b) Applied potential profile including the AST of regular –20% reverse cycle (cycling ranging from –1.3 V vs RHE to 0.5 V vs RHE for 60 000 cycles) and constant durability test of regular condition (at –1.3 V vs RHE for 50 h). (c) Measured LSV curves of pristine NR electrode, NR electrode after AST and after constant test, (d) EIS plots (e) the morphology images of pristine NR electrode, NR electrode after AST and after constant test. (f) The atomic percentage acquired from EDS.

a three-electrode cell (cell A). During the AST, electrochemical measurements including electrochemical active area (ECSA) acquired from cyclic voltammograms (CV), linear sweep voltammetry (LSV) and electrochemical resistance spectroscopy (EIS) were carried out every 1000 cycles in another three-electrode cell. To quantify the electrode performance change, overpotentials at various current densities (η_{100} , η_{400} , η_{800}) were obtained from LSV, among which the time-dependent increase of η_{400} was defined as the degradation rate (mV h^{-1}). Specific electrochemical results are demonstrated in next paragraph.

Figure 2c and Figure S9 displays the LSV comparison of the pristine NR, NR after AST (NR-AST) and NR after CP (NR-CP), in which a 214-mV increase of η_{400} for NR-AST (488 mV) compared to that of NR-CP (274 mV) were acquired. Over 10-time of increased degradation rate of NR-AST (4.76 mV h^{-1}) to that of NR-CP (0.473 mV h^{-1}) indicates that the AST condition accelerated the degradation. To reveal the causes from the aspect of electrochemical property, EIS results are shown in Figure 2d, from which the charge transfer resistance and ohm resistance were fitted. R_{ct} and R_Ω of NR-AST are 2.02 and 1.15Ω respectively, much higher than that of NR-CP (0.51Ω R_{ct} and 0.87Ω for R_Ω), which may be resulted from the deterioration of NR interface or structure. For further assessing the surface and structural degradation, scanning electron microscope (SEM) and Energy

Dispersive X-ray Spectroscopy (EDS) were conducted. As shown in Figure 2e and Figure S10, NR-AST were featured by severe Ru-layer depletion and Ni substrate exposure. Figure 2f and Figures S11 and S12 demonstrated a decreased Ru atomic percentage from 4.79 to 0 at.%, which verified the total detachment of Ru as well. At the same time, apparent cracks of NR-AST were observed in Figure 2e and Figure S17, which suggested the damage of Ni substrate.

2.2 | Electrochemical Behavior and Morphology Evolutions

To gain more deep insight into the degradation dynamics of NR-AST, evolution of the overpotentials, ECSA, R_{ct} and R_Ω were plotted and shown in Figure 3a,b. The η_{400} increased rapidly at a rate of 102.8 mV h^{-1} during the initial 2000 cycles (250 to 422 mV), followed by a much slower increase of 1.4 mV h^{-1} from 2000 to 60 000 cycles (422 to 488 mV). At the same time, the ECSA increased from 0 to 20 000 cycles (0.52 to 0.72) then declined from 20 000- to 60 000 cycles (0.72 to 0.53). Given the distinctly different trends with 2000- and 20 000-cycle as transition nodes, the degradation process was divided into three stages for detailed analysis: 0–2000 (Stage 1), 2000–20 000 (Stage 2) and

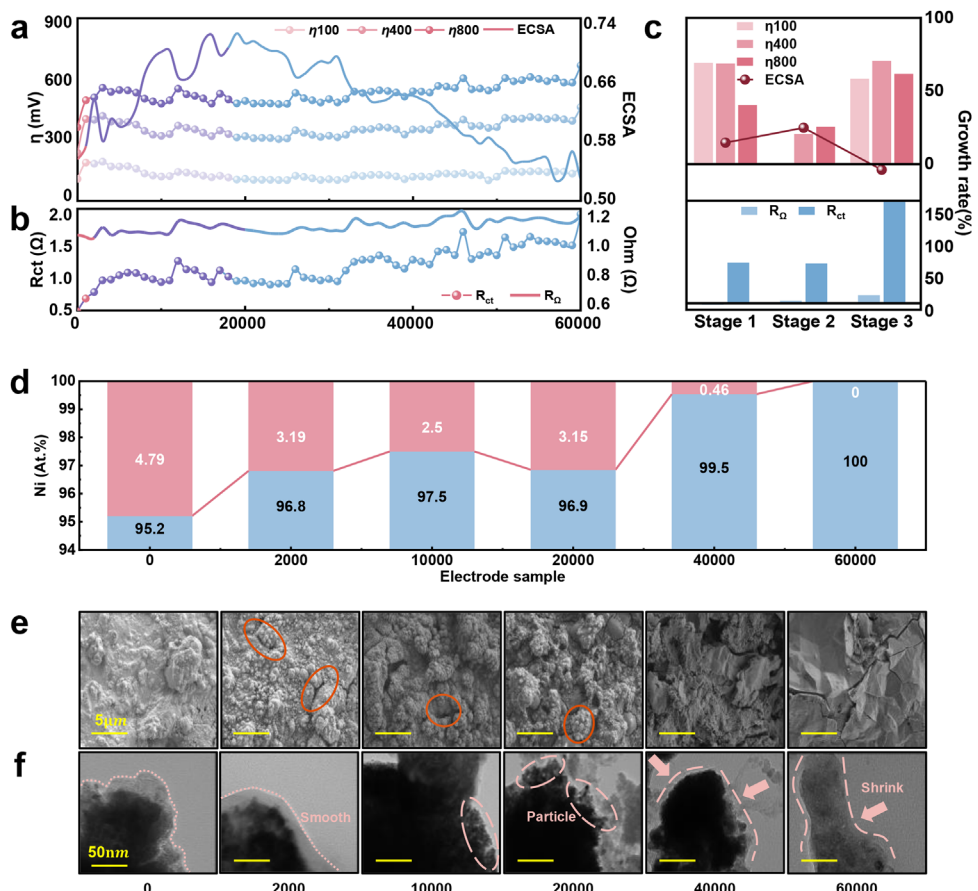


FIGURE 3 | Performance changes and morphology features in different degradation stage. (a) The overpotential curves at 100, 400, and 800 mA cm^{-2} and ECSA curve. (b) The charge transport resistance curve and ohm resistance curve. (c) The degradation rate of overpotentials, ECSA, charge transport resistance and ohm resistance compared with the pristine state. (d) The atomic percentage of surface acquired from EDS. (e) The SEM images of electrode surface at different stages. (f) The TEM images of Ru particles at different stages.

20 000–60 000 (Stage 3) cycles (Figure 3a,b; Figures S13–S16, Table S4).

In stage 1 η_{400} was increased from 250 to 422 mV, indicating the initial reduction of catalytic activity. At the same time ECSA was increased from 0.54 to 0.64, suggesting the probable morphology changes. R_{ct} was increased simultaneously from 0.48 to 0.79 Ω , which is correlated to the surface deterioration. By contrast, in stage 2 η_{400} was reduced from 422 mV to 337, meaning the activity recovery behavior. Meanwhile the ECSA and R_{ct} were risen from 0.64 to 0.72 and from 0.79 to 0.97 Ω , respectively, meaning that similar morphology features changed accompanied by continuous surface deterioration in stage 2. However, η_{400} was found to rebound to 488 mV in stage 3, namely the re-decrease of catalytic activity. Meanwhile the ECSA was decreased to 0.53 and R_{ct} was risen to 2.01 Ω , which demonstrated that converse morphology change occurred with the further surface degradation.

Figure 3d–f and Figure S10 presented the morphology and elemental distribution evolution of the degradation process acquired by EDS, SEM and TEM. In stage 1, dense and small-particle Ru layer were observed to transformed into cracked and larger-particle layer, along with the reduction of Ru atomic percentage from 4.79 to 3.19 at.%. Based on the previous investigation on

Ru-based catalyst [35–37], Ru-species loss had been validated to reduce the catalytic activity, which implies that decreased Ru in stage 1 was responsible for the increase of η and R_{ct} . In addition, the morphology changes during the Ru loss were inferred to result in the increased ECSA. In stage 2, notable sophisticated structures and defects were observed, along with outer smaller-scale Ru particle in TEM images. We conclude that the newly formed particles caused the increased ECSA. At the same time, Ru atomic percentage was found to recover back to 3.15 at.%, meaning the probable Ru redeposition during stage 2, which was deduced to result in the decreased η . Stage 3 is featured by the gradual depletion of the structures formed in stage 2 and total exposure of Ni substrate, explaining the increased η and R_{ct} . The outer small-particles were no longer visible and size of the core particle were observed to shrink. Ru atomic percentage was declined to 0 at.% eventually, confirming the Ru depletion, which could be the cause of ECSA decline.

2.3 | Solution and Interface Evolutions

To further ascertain the above dynamic process, evolutions of solution and electrode interface were characterized. Compositional evolution acquired by Inductively Coupled Plasma Optical Emission Spectrometry/Mass Spectrometry (ICP-MS) of

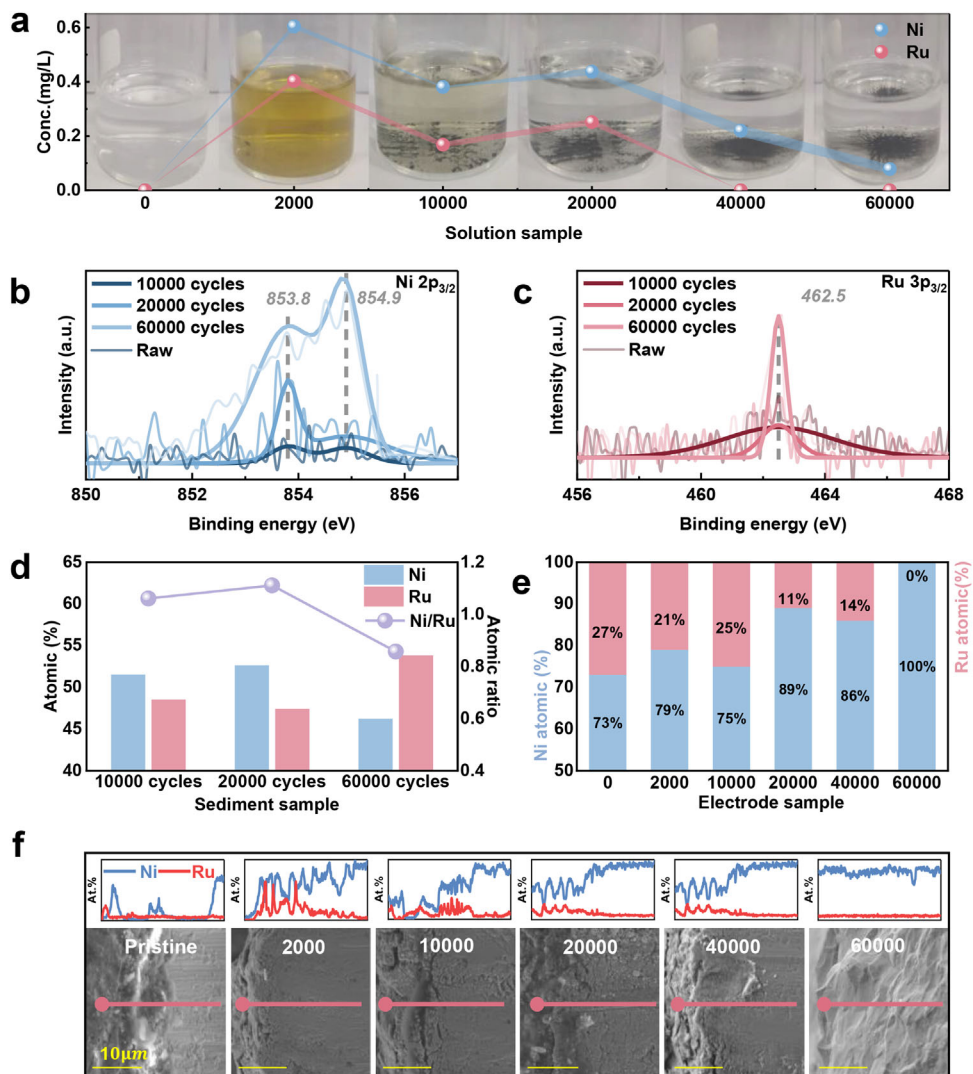


FIGURE 4 | Metal ion concentration in testing solution, elemental composition and electrode cross-section elemental distribution in different degradation stages. (a) Recorded appearance images and corresponding elemental concentration in working solution at different stages acquired from MS-ICP. Curve-fitted XPS results of (b) Ni 2p and (c) Ru 3p in precipitates for 10 000-, 20 000-, and 60 000-cycle sample. (d) The atomic percentage of precipitates at different stages acquired from XPS. (e) The atomic percentage within 5 μm of the electrode surface acquired from EDS. (f) The cross-section EDS results at different stages.

electrolyte solution in cell A were conducted along with the appearance records. X-ray photoelectron spectroscopy (XPS) was employed for detection of the precipitates composition, and the spectroscopy results were normalized to eliminate the impact of C peak signal (284.8 eV). More than that, to assist in understanding the interface evolution, elemental distributions in the depth direction of NR-AST were attained by cross-sections SEM and EDS line scan. At the same time the cumulative atomic percentages within 5 μm starting from the outer layer were acquired from the EDS results.

Figure 4a-d and Figure S18 displays the evolution of the electrolyte solution and XPS results of precipitates. Regarding the evolution of solution appearance, change from colorless to orange was observed in stage 1, consistent with the phenomenon from Holmin et al. [15]. From the ICP-MS result, Ru concentration were found to rise from 0 to 0.60 mg/L (Table S5), which had been validated to be the formation of Ru species with higher

oxidation states (Ru^{7+} , Ru^{8+} etc.) [38]. It is worth noting that the Ni concentration was found to rises from 0 to 0.40 mg/L, indicating the probable dissolution of Ni substrate in stage 1. Stage 2 witnessed the disappearance of orange to light green then back to colorless, with the presence of dark precipitates at the cell bottom. Concentration of Ru and Ni was increased to 0.25 and 0.43 mg/L, respectively. Previous research had verified the transition to green to be the gradual presence of Ni with high oxidation state by Ultraviolet-visible spectroscopy (UV-vis) [39]. Regarding the XPS result, the precipitates were inspected to be the mixture of metal Ni (853.8 and 854.9 eV) and RuO_2 (462.5 eV), meaning the deposition of free Ni and Ru in stage 2. Thus, we inferred that the sophisticated structures in stage 2 mentioned in the last section were resulted from the deposition of Ni and Ru as well. In stage 3, no apparent color change of the electrolyte solution was found. Concentration of Ni and Ru were decreased from 0.43 to 0.07 mg/L and from 0.25 mg/L to 0, respectively. Meanwhile, increased precipitates in the cell bottom

were observed, along with the XPS intensity rises of the Ni and RuO₂ peaks from 20 000- to 60 000-cycle. Therefore, formation of Ni and RuO₂ precipitate was responsible for the concentration decrease of Ni and Ru. Additionally, considering the elemental proportion in Figure 4d, the ratio of Ni to Ru was decreased from 1.1 to 0.85, meaning the greater share of the Ru deposition process. As a result, we concluded that the dissolution of Ru was the main degradation process in stage 3, accompanied by the deposition of the Ni and Ru ions.

Figure 4e,f demonstrates the results of cross-section images and atomic percentages. In stage 1, disappearance of Ru signal at the outmost layer was observed in line scan results. According to the elemental share result in Figure 4e, the Ru atomic percentage was decreased from 27 to 21 at.% at the out-layer, which has been attributed to the Ru electrochemical dissolution. In stage 2, multilayer alternations of Ni and Ru signals were observed accompanied by outward shifting of the Ni signals, which confirmed the co-deposition process of Ni and Ru in stage 2. In stage 3, no evident Ru signal was detected, with the cross-section turning sleek. With the Ru atomic percentage declining from 27 to 0 at.%, the Ru-species was confirmed to be totally consumed. Therefore, based on the analysis above, the three-stage process of the NR electrode during AST can be summarized as: (i) dissolution of surface Ru; (ii) dissolution of Ni substrate and deposition of free Ru and Ni; (iii) dissolution of Ru and deposition of free Ru and Ni. The detailed evolution mechanisms in each stage will be discussed in the next section.

2.4 | Degradation Mechanism and Pathway Analysis

To ascertain the stage-evolution mechanisms from thermodynamic state of Ni and Ru in each stage, Pourbaix diagrams were referred. Converting the reference hydrogen potential (RHE) in AST into standard hydrogen electrode (SHE) utilized in Pourbaix diagrams based on Nernst equation, AST-potential of -0.37 V vs SHE and 1.43 V vs SHE was acquired.

$$E(\text{SHE}) = E(\text{RHE}) + 0.0591 \times \text{pH} + 0.098 \text{ V}, \text{pH} = 14 \quad (1)$$

According to the diagram in Figure 5a, Ru-species were supposed to be the mixture of metal Ru and RuO₂ at -0.37 V vs SHE and electrochemically dissolved into HRuO₅⁻ at 1.43 V vs SHE, validating the dynamic process of Ru dissolution and deposition. Therefore, we concluded that the main behavior in stage 1 was the dynamic cycling of 2-s Ru dissolution and 1-s redeposition in a single cycle, leading to the general trend of Ru-species loss. As for the Ni dissolution, Kim et al. had reported that maintaining the cathodic potential below 1.5 V vs SHE can effectively keep the Ni from oxidation, which was not conforming to the Ni dissolution under 1.43 V vs SHE in this work, illustrating the existence of extra driven force to motivate the Ni dissolution in NR electrode [29, 40].

Yet, a Ni galvanic corrosion origin from the galvanic coupling mechanism had been reported by Liu et al. [42]. The galvanic corrosion was validated to result from the coexistence of Ni and other metal with higher oxidation potential, during which Ni worked as the anode in the galvanic couple and was oxidized

[43–45]. Taking the case as a reference, according to the standard electrode potential acquired from database, the Ru deposition potential of 0.455 V vs. SHE and Ni dissolution potential of -0.257 V vs. SHE fulfilled the condition of galvanic couple, which might result in mutual promotion of Ni dissolution and Ru deposition [15, 35, 46]. Thus, we hypothesized that the galvanic couple of Ni/Ru in KOH could be responsible for the Ni corrosion and Ru deposition. To confirm the rationality, a three-phase galvanic simulation model composed of Ni/Ru/KOH was constructed in COMSOL (Figure S29). Setting the electrode potential at 1.43 V vs SHE, a 0–800 s simulation comparison result was obtained. As is shown in Figure 5b, the electrolyte potential adjacent to Ni (1.15 V vs SHE) was found to be high than that of Ru side (1.13 V vs SHE), making the Ni work as the galvanic anode and be oxidized. Compared with the initial state, apparent Ni loss was observed. Therefore, we concluded that the corrosion of Ni substrate was induced by the Ru/Ni co-exposure to electrolyte after stage 1 (Figure S20). Since the galvanic reaction rate was proportional to the concentration of reactant, the Ni corrosion was supposed to be promoted by the high concentration of free Ru. Yet the finite content of free Ru after stage 2 did not remain high enough to support the continuous happening of the galvanic coupling corrosion, which led to the subsequent process transition from the Ni corrosion to Ru dissolution.

Figure 5c presents the scheme of the degradation pathway in stages based on the above analysis. In the initial stage, dense Ru pre-deposited on the Ni mesh was dissolved into solution under excessive reverse potential, which led to the exposure of underlying Ni substrate and bulk HRuO₅⁻ lost in the solution. (Figures S17 and S19) The above results formed the condition of stage 2, during which the exposed Ni and the comprised the galvanic couple, leading to the simultaneous occurrence of Ni corrosion and Ru deposition. (Figure S20) In stage 2 Ni was corroded into Ni²⁺ and HRuO₅⁻ was redeposited, part of which was deposited back to the electrode surface, thereby sophisticated structures were formed. After a period of cycling, for the high content of HRuO₅⁻ were consumed by the Ni corrosion, the galvanic reaction was no longer supported, and the Ru-species continued to be dissolved. As a result, the sophisticated structures formed from galvanic reaction were re-dissolved into solution in stage 3, then reduced into precipitates under the regular potential, which occurred until the Ru layer on surface was totally consumed, leaving the corroded Ni substrate exposed distinctly.

2.5 | Sensitivity on the RC Amplitude

Aiming to further reveal the degradation-trigger mechanism of RC, sensitivity of NR electrode to the RC amplitude was investigated in the three-electrode system. By setting the RC amplitude fraction (-20%, -10%, 0%) the reverse potential (1.43 V vs SHE, 0.43 V vs SHE, -0.04 V vs SHE) in the AST protocol was adjusted, after which the post measured electrochemical results of the three-electrode AST were conducted (Figure 6a–c; Figures S21–S25).

Figure 6a–c displayed the LSV, EIS and ECSA results of the samples. η_{400} of the 0%-AST (NR-AST-0) (211 mV) and 10%-AST sample (NR-AST-10) (253 mV) were attained. Increases of NR-AST-0 and NR-AST-10 respectively were 39 and 2 mV

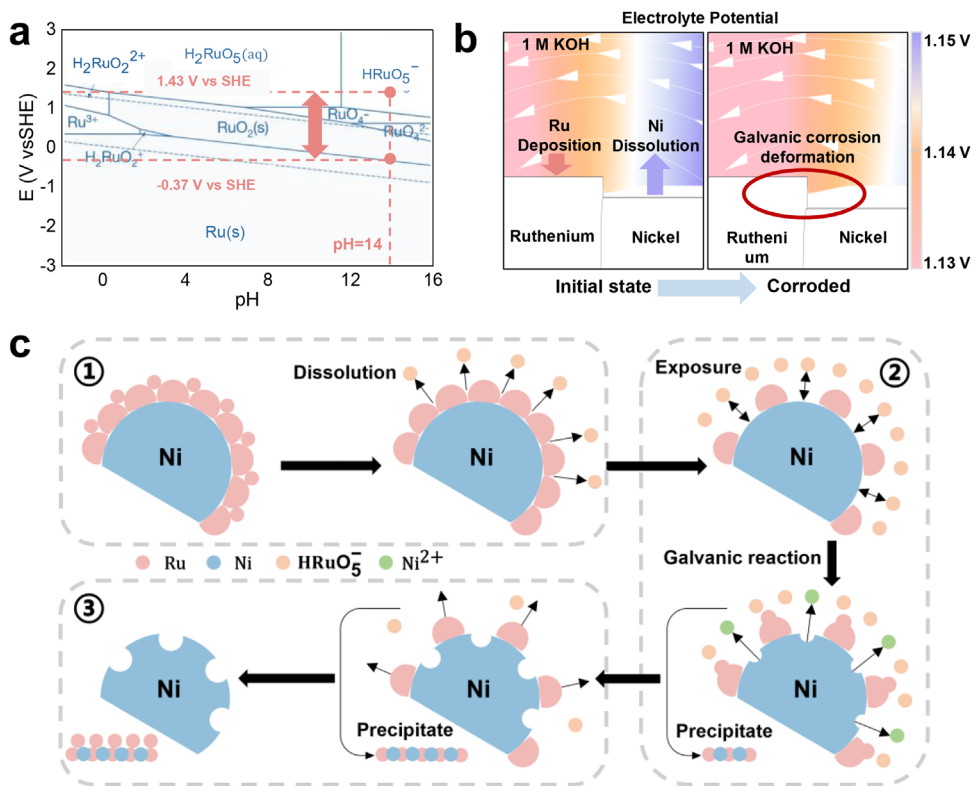


FIGURE 5 | Degradation mechanism illustrated by scheme and simulation results. (a) Pourbaix diagram of Ru [41]. Copyright 2020 Z Wang et al. (b) Simulated galvanic corrosion result at initial state and after a period of 800s. (c) Scheme diagram of the degradation process under AST.

compared with pristine NR, much lower than the 238 mV of 20%-AST sample (NR-AST-20) (Table 1). Thus, declining the reverse potential effectively mitigates the catalytic activity reduction. Based on the EIS result, apparently smaller impedance arcs and horizontal axis intercepts were found, namely less R_{ct} and R_{α} of NR-AST-0 and NR-AST-10 compared with that of NR-AST-20, which suggests that less surface deterioration occurred. At the same time, the apparent slope increase compared with that of NR-AST-20 in Figure 6c indicates that distinct morphology changes occurred under different ASTs. Moreover, corresponding current-controlled AST and EIS were conducted in an alkaline electrolysis system as well, along with the LSV conducted in three-electrode cell at begin of test (BoT) to end of test (EoT), respectively. As is shown in Figure S32a, full-cell voltage was risen significantly from BoT to 20% EoT (from 1.62 to 1.71 V). Identical changing trends of the LSV and EIS in Figure S32b,c were found to be consistent with the above three-electrode test results in Figures 6a,b, which further confirmed the mitigation effect of declining RC fraction.

To ascertain the mitigation mechanism, SEM images and EDS results were presented in Figure 6e,f. Only a few cracks of NR-AST-0 and NR-AST-10 were observed, meaning less corrosion occurred. We inferred that it is the formation of cracks that released more active sites, which led to the ECSA increase. More than that, considering the EDS result, 2.79 at.% and 0.23 at.% of Ru was observed, which further confirmed the higher surface preservation of lower-amplitude AST. Yet according to the Pourbaix diagram, the electrochemical transition from solid Ru

or RuO_2 to ions occurs only under 1.43 V vs SHE (NR-AST-20), at the same time no color changes were observed during the 0%-AST and 10%-AST, indicating that no irreversible oxidation occurred. To prove the oxidation behavior, XPS were conducted to the electrodes. As is shown in Figure 6d, apparent peak of the Ru 3p at 462.5 eV was found of NR-AST-20 compared with the pristine NR, which had been confirmed to be related to the formation of RuO_2 . While no visible changes were observed to the NR-AST-0 and NR-AST-10, meaning that oxidation was not the cause of the surface changes. Referring to a metal surface damage resulting from bubble cavitation and tip-oxidation reported by Lampke et al. and Mo et al. [46, 47]. (Figures S27 and S28), it can be deduced that the Ru loss under 0% and 10% AST can be attributed to bubbles cavitation and stress corrosion during electrolysis, which is inevitable. Furthermore, we concluded that NR-AST-0 suffered from the cavitation by least bubbles, explaining the largest Ru layer preservation (2.79 at.%). For validation, the extended 0% AST was conducted. As shown in Figure S26 and Table 1, only after 200 000 cycles did the η_{400} rise to 293 mV. The degradation rate was calculated to be 0.257 mV h^{-1} , much lower than 4.756 mV h^{-1} of NR-AST-20, which illustrates the lifetime extension effect of 0%-AST to NR. The result demonstrates that under different RC conditions the NR exhibits various degradation behavior, thereby affecting the electrode lifetime. The above investigations provide with mechanistic idea on the design of RC-tolerant electrode in futural RE-AWE development. More than that, from the aspect of electrolysis system, through voltage-limitation operation the RC is largely suppressed, which could be considered as an essential mitigation strategy.

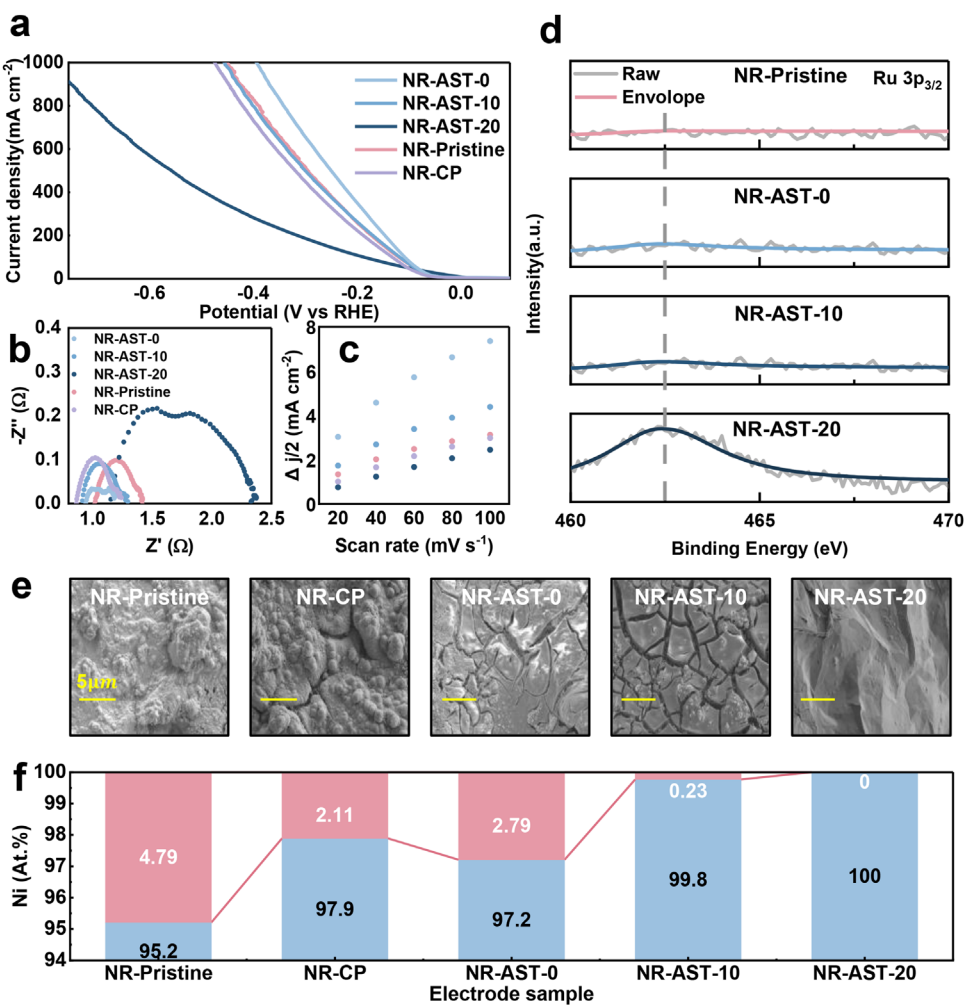


FIGURE 6 | Performance and morphology changes under different AST profiles. (a) Measured LSV curves of pristine NR electrode, NR electrode after AST of different reverse voltage and after constant test. (b) Measured EIS and (c) measure ECSA. (d) The XPS comparison of Ru 3p of the pristine sample and AST samples. (e) The SEM images of electrode surface after different tests. (f) The atomic percentage of surface under different test conditions acquired from EDS.

TABLE 1 | Overpotential and degradation rate of tested samples.

Sample	Overpotential @Current density/mV			Degradation rate /mV.h ⁻¹ @400 mA cm ⁻²
	100 mA cm ⁻²	400 mA cm ⁻²	800 mA cm ⁻²	
Pristine	114.32	250.33	383.54	/
Constant 50h ^{a)}	126.64	273.97	414.86	0.473
NR-AST-20 60 000 cycles	181.27	488.10	704.38	4.756
NR-AST-10 60 000 cycles	111.85	253.57	394.86	0.0648
NR-AST-0 60 000 cycles	102.41	211.05	335.50	-0.7856
NR-AST-0 100 000 cycles	137.89	273.42	382.63	0.2771
NR-AST-0 200 000 cycles	143.18	293.16	434.85	0.2570

^{a)}50 h is equal to the test time of 60 000 cycles in AST.

3 | Conclusions

We introduced a two-step “RC-like” AST protocol to simulate the regular-reverse cycling input. Through the combination

of time-resolved electrochemical measurements, morphological and compositional analysis, the whole degradation behavior of NR was demonstrated and elucidated. Initially, under the excess reverse potential, dissolution of surface Ru occurred, leading

to the formation of surface defects and free Ru ions in the electrolyte. Subsequently, promoted by the above defects and free ions, Ni substrate was exposed and corroded under the Ni-Ru-electrolyte coupled galvanic reaction. Eventually, suffered from the alternation of the above dissolving and galvanic reaction, Ru layer was totally depleted and the Ni substrate was severely damaged. In addition, aiming to ascertain the trigger of the cascade degradation and attain corresponding mitigation idea, sensitivity of NR to the RC amplitude was investigated. Reducing the RC fraction from 20% to 0%, degradation rate was significantly suppressed from 4.756 to 0.257 mV h⁻¹. We deduced that it is the inhibition of initial Ru dissolution that kept NR from subsequent corrosion. The above results demonstrate the variation of RC-induced degradation behavior for Ni-X electrodes under different RC conditions. Through the investigations we contribute mechanistic insight on the RC-induced degradation and provide with reference toward the futural RC-tolerant electrode design utilized in RE-AWE.

4 | Experimental

4.1 | Electrode Preparation

The Ni mesh with in situ deposited Ru (JP New Energy, AZ-46/19, Table S1 and Table S2) was selected as the studied object to investigate the electrode degradation during long-time regular-reverse potential cycles. The pristine NR electrode obtained by electrodeposition show an inhomogeneous profile of Ru uniformly distributed in the outer layer of Ni (Figure S2). The sample demonstrated good reproducibility in terms of electrochemical properties. (Figure S1) Basic stability was tested under RC of 100 mA cm⁻² for 100 s (Figure S3). The Ru showed distinct unstable property and free ions presented as orange ruthenate shown in Figure S3, which was transformed into ruthenate hydroxide subsequently based on Pourbaix diagram in Figure 5b.

4.2 | AST Setup and Electrochemical Measurement

The AST was designed based on the alternation of regular and reverse operation. 100 mA cm⁻² was chosen as the regular condition while the -20% of the regular value namely -20 mA cm⁻² was set as the reverse condition. To facility the mechanism study in this work, potential-controlled AST were employed in the three-electrode test due to stronger redox-correlation compared with current-controlled AST. The potential cycling from 100 and -20 mA cm⁻² was measured to be -1.3 V vs RHE and 0.5 V vs RHE, respectively (Figure S4; Figure 2a,b). In the contrast, to meet the practical RC operation in the two-electrode system, current-controlled AST was utilized in the alkaline electrolyzer experiment.

As for the duration time of each stage, considering that the response time of RC is usually within hundred milliseconds, to maximize the impact density of RC and shorten the test duration, 1 and 2s were set as the single-step length of RC step and regular step, respectively. Specific selecting principle of parameters are demonstrated in Figures S30 and S31, Tables S8 and S9 and Parameter selection of AST.

A glass three-electrode electrochemical cell containing 1 M KOH system using the NR electrode as working electrode (Figure S3) was employed, while a 2*2 mm platinum plate as the counter electrode and a Hg/HgO reference electrode.

During the AST process, electrochemical measurements comprising cyclic voltammograms (CV), linear sweep voltammetry (LSV) and electrochemical resistance spectroscopy (EIS) were performed every 1000 cycles. (CorrTest CS310M) Prior to each measurement, the electrode was activated by performing CVs until a stable voltammogram was obtained. The double-layer capacitance was determined by conducting CV measurements at 5 different scan rates (20 to 100 mV s⁻¹) within the non-Faradaic region (-0.7 to -0.8 V vs. RHE), thereby the electrochemical active surface area (ECSA) was calculated based on the ratio of the double-layer capacitance to the theoretical specific double-layer capacitance (40 μF/cm²). The LSVs were conducted from -0.7 to -2.7 V with the scan rate of 5 mV s⁻¹ (Figure S6). EIS measurements were conducted at -1.2 V (vs. RHE) with an amplitude of 10 mV and frequencies ranging from 100 000 to 0.1 Hz.

The above measured potential values were converted to the reversible hydrogen electrode (RHE) scale. Calculation of R_{ct} and R_{Ω} were fitted from the equivalent circuit model (ECM) shown in Figure S5. R_{Ω} drop compensation was performed based on the measured R_{Ω} resistance from electrochemical resistance spectroscopy (EIS), calculated using Equation:

$$V(\text{vs.RHE}) = V_{\text{measured}} + 0.9268 - 0.85 \times i_{\text{measured}} \times R \quad (2)$$

4.3 | Configuration of the Electrolyzer Validation Experiment

A zero-gap single-cell (Active area: 1 cm²) consisting of the current collectors, Ni-plated polar plates with serpentine flow-channel, electrodes and a commercial Agfa-500 diaphragm (Thickness: 500 μm), was assembled and fastened by six torque-set bolts (Torque: 30 Nm*6), where the Ni mesh (Mesh count: 46, Wire diameter: 0.1 mm) and the studied NR electrode were used as anode and cathode, respectively. An NGI36100 programmable DC power supply was used to conduct the current-controlled AST (-100 mA for 2 s and 20 mA for 1 s) for 60 000 cycles. Voltage curve was measured at 80°C, with 7 M KOH solution circulating in the alkaline electrolysis system at 15 mL/min. Full-cell EIS were employed before and after the AST (Frequency:100 000–0.1 Hz, Potential: open circuit potential, Amplitude:10 mV). The LSV of the studied NR were measured in the three-electrode cell with 1 M KOH solution before and after the test.

4.4 | Physical Characterization

The SEM images were acquired using a JSM-7900F instrument with an accelerating potential of 3 kV. Energy dispersive spectroscopy (EDS) was conducted with a Super X detector. The probed electrode samples of different stages were prepared by imposing AST for corresponding length. (Figure S5)

The tested solution was sampled for 10 μL every 1000 cycles to ensure that the effect of sampling on the test solution is minimized, then diluted into 6 mL and kept in vials. (Figure S5) Solution samples at different stages were characterized for 3 times with Inductively Coupled Plasma Optical Emission Spectrometry/Mass Spectrometry (MS-ICP). Values in Figure 4a is the average of the three results. ICP-OES/MS measurement were acquired using Agilent 7850(MS) instrument.

XPS measurements were made with a Thermo Fisher ESCALAB 250Xi system, utilizing Al K α radiation ($\text{hv} = 1486.6 \text{ eV}$) as the excitation source. Binding energies for the high-resolution spectra were adjusted according the C 1s peak to 284.8 eV. The probed precipitate samples of different stages were prepared by imposing AST for corresponding length as well.

4.5 | Dynamic Dissolution/Deposition and Osterwalder Ripening

Considering the existence of reciprocating condition, the transient dynamic dissolution and deposition of Ru or RuO₂ may affect the degradation result. To mitigate the effect, short-step AST (500 cycles as measurement step for 1500 cycles in total) is conducted to find out the minimum measurement step not influenced by the dynamic process. As is shown in Figure S8, the ECSA of the tested cathode underwent specific decreasing and then increasing trend, consistent with the difference of LSV curves. At the same time, the SEM comparison between pristine sample and 500-cycle sample (Figure S7) shows that the surface Ru particles are roughened and fresh deposited skeletonized Ru particles adhered on the larger particle, confirming the existence of dynamic dissolution-deposition process, namely the Osterwalder ripening [48, 49]. Therefore, setting the measure step for more than 500 cycles can effectively neglect the effect of transient dynamic process.

Acknowledgements

The authors acknowledge the financial support from National Key R&D Program of China, Nos. 2022YFB4002303, National Natural Science Foundation of China, Grant Nos. 52241701 and 52307249, Science and technology projects of Shaanxi Province Grant Nos. 2024GX-ZDCYL-04-02 and 2024QCY-KXY-133, Fundamental Research Funds for the Central Universities at Tongji University.

Conflicts of Interest

The authors declare no conflicts of interest.

Data Availability Statement

The data that support the findings of this study are available from the corresponding author upon reasonable request.

References

- H. Zhao and Z.-Y. Yuan, "Progress and Perspectives for Solar-Driven Water Electrolysis to Produce Green Hydrogen," *Advanced Energy Materials* 13, no. 16 (2023): 2300254, <https://doi.org/10.1002/aenm.202300254>.
- M. Yu, E. Budiyanto, and H. Tüysüz, "Principles of Water Electrolysis and Recent Progress in Cobalt-, Nickel-, and Iron-Based Oxides for the Oxygen Evolution Reaction," *Angewandte Chemie International Edition* 61, no. 1 (2022): 202103824, <https://doi.org/10.1002/anie.202103824>.
- H. Shin, D. Jang, S. Lee, H.-S. Cho, K.-H. Kim, and S. Kang, "Techno-economic Evaluation of Green Hydrogen Production With Low-temperature Water Electrolysis Technologies Directly Coupled With Renewable Power Sources," *Energy Conversion and Management* 286 (2023): 117083, <https://doi.org/10.1016/j.enconman.2023.117083>.
- I. M. Perović, S. D. Mitrović, S. M. Brković, and I. A. Pašti, "Advances in Nickel-Based Catalysts for Alkaline Water Electrolysis: Comprehensive Review of Current Research Direction for HER and OER Applications," *The Chemical Record* 25 (2025): 202500049.
- H. Li, Y. Zhang, Y. Chen, et al., "Leveraging Iron in the Electrolyte to Improve Oxygen Evolution Reaction Performance: Fundamentals, Strategies, and Perspectives," *Angewandte Chemie International Edition* 64, no. 8 (2025): 202423071, <https://doi.org/10.1002/anie.202423071>.
- C. Li, B. Kim, Z. Li, et al., "Direct Electroplating Ruthenium Precursor on the Surface Oxidized Nickel Foam for Efficient and Stable Bifunctional Alkaline Water Electrolysis," *Advanced Materials* 36, no. 31 (2024): 2403151, <https://doi.org/10.1002/adma.202403151>.
- N. S. Hassan, A. A. Jalil, S. Rajendran, et al., "Recent Review and Evaluation of Green Hydrogen Production Via Water Electrolysis for a Sustainable and Clean Energy Society," *International Journal of Hydrogen Energy* 52 (2024): 420–441, <https://doi.org/10.1016/j.ijhydene.2023.09.068>.
- M. Du, X. Lv, Z. Yong Cao, Q. Jun Wang, and J.-E. Qu, "Review of Catalytic Electrodes Containing Iron-Cobalt-Nickel Composite Components for Water Electrolysis," *Chemphyschem* 26, no. 3 (2025): 202400500, <https://doi.org/10.1002/cphc.202400500>.
- D. Christopher Selvam, Y. Devarajan, T. Raja, and S. Vickram, "Advancements in Water Electrolysis Technologies and Enhanced Storage Solutions for Green Hydrogen Using Renewable Energy Sources," *Applied Energy* 390 (2025): 125849, <https://doi.org/10.1016/j.apenergy.2025.125849>.
- S. Bi, Z. Geng, Y. Wang, et al., "Multi-Stage Porous Nickel-Iron Oxide Electrode for High Current Alkaline Water Electrolysis," *Advanced Functional Materials* 33, no. 31 (2023): 2214792, <https://doi.org/10.1002/adfm.202214792>.
- J. Jiang, X.-L. Zhou, H.-G. Lv, H.-Q. Yu, and Y. Yu, "Bimetallic-Based Electrocatalysts for Oxygen Evolution Reaction," *Advanced Functional Materials* 33, no. 10 (2023): 2212160, <https://doi.org/10.1002/adfm.202212160>.
- S. Angizi, M. Nankali, A. Foroozan, et al., "3D Bimetallic Platinum-Nickel Electrodes for Electro-Oxidation of Glycerol at Ambient Conditions," *Advanced Functional Materials* 35, no. 14 (2025): 2420622, <https://doi.org/10.1002/adfm.202420622>.
- J. Divisek, R. Jung, and D. Britz, "Potential Distribution and Electrode Stability in a Bipolar Electrolysis Cell," *Journal of Applied Electrochemistry* 20, no. 2 (1990): 186–195, <https://doi.org/10.1007/BF01033594>.
- A. T. Kuhn and J. S. Booth, "Electrical Leakage Currents in Bipolar Cell Stacks," *Journal of Applied Electrochemistry* 10, no. 2 (1980): 233–237, <https://doi.org/10.1007/BF00726091>.
- S. Holmin, L.-Å. K. Näslund, Á. S. Ingason, J. Rosen, and E. Zimmerman, "Corrosion of Ruthenium Dioxide Based Cathodes in Alkaline Medium Caused by Reverse Currents," *Electrochimica Acta* 146 (2014): 30–36, <https://doi.org/10.1016/j.electacta.2014.09.024>.
- L.-Å. Näslund, Á. S. Ingason, S. Holmin, and J. Rosen, "Formation of RuO(OH)₂ on RuO₂-Based Electrodes for Hydrogen Production," *The Journal of Physical Chemistry C* 118, no. 28 (2014): 15315–15323, <https://doi.org/10.1021/jp503960q>.
- R. E. White, C. W. Walton, H. S. Burney, and R. N. Beaver, "Predicting Shunt Currents in Stacks of Bipolar Plate Cells," *Journal of The Electrochemical Society* 133, no. 3 (1986): 485, <https://doi.org/10.1149/1.2108606>.
- Y. Uchino, T. Kobayashi, S. Hasegawa, et al., "Dependence of the Reverse Current on the Surface of Electrode Placed on a Bipolar Plate in

- an Alkaline Water Electrolyzer," *Electrochemistry* 86, no. 3 (2018): 138–144, <https://doi.org/10.5796/electrochemistry.17-00102>.
19. N. Guruprasad, J. van der Schaaf, and M. T. de Groot, "Unraveling the Impact of Reverse Currents on Electrode Stability in Anion Exchange Membrane Water Electrolysis," *Journal of Power Sources* 613 (2024): 234877, <https://doi.org/10.1016/j.jpowsour.2024.234877>.
 20. N. Tsukase, T. Araki, A. A. Haleem, K. Nagasawa, Y. Kuroda, and S. Mitsushima, "Numerical Simulation of the Distribution of Reverse Currents in a Practical Alkaline Water Electrolysis Stack Immediately After Electrolysis," *International Journal of Hydrogen Energy* 49 (2024): 701–712, <https://doi.org/10.1016/j.ijhydene.2023.09.006>.
 21. S.-M. Jung, Y. Kim, B.-J. Lee, et al., "Reverse-Current Tolerance for Hydrogen Evolution Reaction Activity of Lead-Decorated Nickel Catalysts in Zero-Gap Alkaline Water Electrolysis Systems," *Advanced Functional Materials* 34, no. 27 (2024): 2316150, <https://doi.org/10.1002/adfm.202316150>.
 22. K. Oda, Y. Kuroda, and S. Mitsushima, "Investigation of Charge-Discharging Behavior of Metal Oxide-Based Anode Electrocatalysts for Alkaline Water Electrolysis to Suppress Degradation due to Reverse Current," *Electrocatalysis* 14, no. 3 (2023): 499–510, <https://doi.org/10.1007/s12678-023-00815-0>.
 23. Y. Uchino, T. Kobayashi, S. Hasegawa, et al., "Relationship between the Redox Reactions on a Bipolar Plate and Reverse Current after Alkaline Water Electrolysis," *Electrocatalysis* 9, no. 1 (2018): 67–74, <https://doi.org/10.1007/s12678-017-0423-5>.
 24. A. Farmani, F. Fahimi, and F. Nasirpour, "Relationship Between Degradation Mechanism and Water Electrolysis Efficiency of Electrodeposited Nickel Electrodes," *Npj Materials Degradation* 9, no. 1 (2025): 25, <https://doi.org/10.1038/s41529-025-00572-z>.
 25. G. Wang, H. Li, F. Babbe, et al., "Probing Electrode Transformation Under Dynamic Operation for Alkaline Water Electrolysis," *Advanced Energy Materials* 15, no. 28 (2025): 2500886, <https://doi.org/10.1002/aenm.202500886>.
 26. M. Mehdi, B.-S. An, H. Kim, et al., "Rational Design of a Stable Fe-rich Ni-Fe Layered Double Hydroxide for the Industrially Relevant Dynamic Operation of Alkaline Water Electrolyzers," *Advanced Energy Materials* 13, no. 25 (2023): 2204403, <https://doi.org/10.1002/aenm.202204403>.
 27. B. Zhang, L. Wang, Z. Cao, et al., "High-valence Metals Improve Oxygen Evolution Reaction Performance by Modulating 3d Metal Oxidation Cycle Energetics," *Nature Catalysis* 3, no. 12 (2020): 985–992, <https://doi.org/10.1038/s41929-020-00525-6>.
 28. Q. Sha, S. Wang, L. Yan, et al., "10,000-h-stable intermittent alkaline seawater electrolysis," *Nature* 639, no. 8054 (2025): 360–367, <https://doi.org/10.1038/s41586-025-08610-1>.
 29. Y. Kim, S.-M. Jung, K.-S. Kim, et al., "Cathodic Protection System Against a Reverse-current After Shut-Down in Zero-gap Alkaline Water Electrolysis," *JACS Au* 2, no. 11 (2022): 2491–2500, <https://doi.org/10.1021/jacsau.2c00314>.
 30. E. Kuhnert, V. Hacker, and M. Bodner, "A Review of Accelerated Stress Tests for Enhancing MEA Durability in PEM Water Electrolysis Cells," *International Journal of Energy Research* 2023, no. 1 (2023): 3183108.
 31. Y. C. Tan, W. K. Quek, B. Kim, S. Sugiarto, J. Oh, and D. Kai, "Pitfalls and Protocols: Evaluating Catalysts for CO₂ Reduction in Electrolyzers Based on Gas Diffusion Electrodes," *ACS Energy Letters* 7, no. 6 (2022): 2012–2023, <https://doi.org/10.1021/acsenergylett.2c00763>.
 32. E. Kuhnert, K. Mayer, M. Heidinger, C. Rienessl, V. Hacker, and M. Bodner, "Impact of Intermittent Operation on Photovoltaic-PEM Electrolyzer Systems: A Degradation Study Based on Accelerated Stress Testing," *International Journal of Hydrogen Energy* 55 (2024): 683–695, <https://doi.org/10.1016/j.ijhydene.2023.11.249>.
 33. P. Aßmann, A. Gago, P. Gazdzicki, K. Friedrich, and M. Wark, "Toward Developing Accelerated Stress Tests for Proton Exchange Membrane Electrolyzers," *Current Opinion in Electrochemistry* 21 (2020): 225–233.
 34. A. Z. Tomić, I. Pivac, and F. Barbir, "A Review of Testing Procedures for Proton Exchange Membrane Electrolyzer Degradation," *Journal of Power Sources* 557 (2023): 232569.
 35. N. Hodnik, P. Jovanovic, A. Pavlisic, et al., "New Insights Into Corrosion of Ruthenium and Ruthenium Oxide Nanoparticles in Acidic Media," *The Journal of Physical Chemistry C* 119, no. 18 (2015): 10140–10147, <https://doi.org/10.1021/acs.jpcc.5b01832>.
 36. M. Minichová, T. Priamushko, M. Zlatar, K. Mayrhofer, and S. Cherevko, "pH Dependence of Noble Metals Dissolution: Ruthenium," *ChemElectroChem* 12, no. (9) 2025: 202400651.
 37. D. Kutyła, K. Kołczyk-Siedlecka, A. Kwiecińska, K. Skibińska, R. Kowalik, and P. Źabiński, "Preparation and Characterization of Electrodeposited Ni-Ru Alloys: Morphological and Catalytic Study," *Journal of Solid State Electrochemistry* 23, no. 11 (2019): 3089–3097.
 38. G. W. Murphy, "Potential-pH Diagrams: Atlas of Electrochemical Equilibria in Aqueous Solutions," By Marcel Pourbaix James A Franklin, *Transl Centre Belge D'Etude De La Corrosion (CEBELCOR)* 154, no. 3756 (1966): 644.
 39. N. Zhang, J. Brugger, B. Etschmann, Y. Ngothai, and D. Zeng, "Thermodynamic Modeling of Poorly Complexing Metals in Concentrated Electrolyte Solutions: An X-Ray Absorption and UV-vis Spectroscopic Study of Ni(II) in the NiCl₂-MgCl₂-H₂O System," *PLoS ONE* 10, no. 4 (2015): 0119805.
 40. M. Alsabet, M. Grden, and G. Jerkiewicz, "Electrochemical Growth of Surface Oxides on Nickel. Part 2: Formation of β -Ni(OH)₂ and NiO in Relation to the Polarization Potential," *Polarization Time, and Temperature Electrocatalysis* 5, no. 2 (2014): 136–147.
 41. Z. Wang, X. Guo, J. Montoya, and J. K. Nørskov, "Predicting Aqueous Stability of Solid With Computed Pourbaix Diagram Using SCAN Functional," *Npj Computational Materials* 6, no. 1 (2020): 160, <https://doi.org/10.1038/s41524-020-00430-3>.
 42. T. Liu, X. Wang, X. Jiang, et al., "Mechanism of Corrosion and Sedimentation of Nickel Electrodes for Alkaline Water Electrolysis," *Materials Chemistry and Physics* 303 (2023): 127806, <https://doi.org/10.1016/j.matchemphys.2023.127806>.
 43. Y. Y. Malinkina, E. V. Chudakov, and V. P. Leonov, "The Influence of Ruthenium on Structure, Corrosion and Mechanical Properties, and Fatigue Characteristics of Titanium α -alloys in Corrosive Environment," *Inorganic Materials: Applied Research* 8, no. 6 (2017): 906–913, <https://doi.org/10.1134/S2075113317060090>.
 44. N. N. Tshilwane and J. W. van der Merwe, "Stress Corrosion Cracking of Laser Alloyed 304L Stainless Steel With Ru in Hot Chloride Solution," *Surface and Coatings Technology* 347 (2018): 414–419, <https://doi.org/10.1016/j.surfcoat.2018.05.020>.
 45. I. Bouessay, A. Rougier, P. Poizot, J. Moscovici, A. Michalowicz, and J.-M. Tarascon, "Electrochromic Degradation in Nickel Oxide Thin Film: A Self-discharge and Dissolution Phenomenon," *Electrochimica Acta* 50, no. 18 (2005): 3737–3745, <https://doi.org/10.1016/j.electacta.2005.01.020>.
 46. T. Lampke, D. Dietrich, A. Leopold, G. Alisch, and B. Wielage, "Cavitation Erosion of Electroplated Nickel Composite Coatings," *Surface and Coatings Technology* 202, no. 16 (2008): 3967–3974, <https://doi.org/10.1016/j.surfcoat.2008.02.004>.
 47. B. Mo, T. Li, F. Shi, L. Deng, and W. Liu, "Crack Initiation and Propagation Within Nickel-based High-temperature Alloys During Laser-based Directed Energy Deposition: A Review," *Optics & Laser Technology* 179 (2024): 111327, <https://doi.org/10.1016/j.optlastec.2024.111327>.
 48. P. W. Voorhees, "The Theory of Ostwald Ripening," *Journal of Statistical Physics* 38 (1985): 231–252, <https://doi.org/10.1007/BF01017860>.
 49. M. Y. Koroleva and E. V. Yurtov, "Ostwald Ripening in Macro- and Nanoemulsions," *Russian Chemical Reviews* 90, no. 3 (2021): 293, <https://doi.org/10.1070/RCR4962>.

Supporting Information

Additional supporting information can be found online in the Supporting Information section.

Supporting Information: **aenm70519-sup-0001-SuppMat.docx**